The effects of processing parameters on hardness, microstructure and corrosion resistance of AlTiZrNbVCr high-entropy alloy

A.O. Ogunyinka[1], *API* Popoola[1], *S.L* Pityana[3], *ER* Sadiku[1] *OM* Popoola[2]

[1]Chemical, Metallurgical and Materials Engineering, Faculty of Engineering and Built Environment, Tshwane University of Technology, P.M.B. X680, Pretoria, South Africa
[2]Center for Energy and Electric Power, Electrical Engineering, Faculty of Engineering and Built Environment, Tshwane University of Technology,
[3]National Laser Centre, Council for Scientific and Industrial Research, Pretoria, South Africa

Abstract. The high-entropy alloys AlTiZrNbVCr (HEAs) are suitable for many applications due to their light weight, high strength, thermal and oxidation resistance. Traditional fabricating methods for HEAs often introduce defects, affecting their mechanical properties and performance. Advanced manufacturing techniques, including additive manufacturing, have been explored to improve microstructures and mechanical characteristics. In this research, the resistance of HEAs to wear and nano-hardness properties was investigated. The sample of HEAs was fabricated via laser additive manufacturing, while the experimental analysis was performed using an X-ray diffraction system (XRD) and a scanning electron microscope (SEM) equipped with energy-dispersive spectroscopy (EDS). The result shows that sample A has the highest hardness and wear-resistant microstructure when compared with the other samples B and C. The Fast Fourier Transform (FFT) SEM processing image was determined at a length scale of the dendrite structure to be LC 192 μm. HEAs are applicable in solid hydrogen energy storage and submarines, especially in propulsion systems where space is limited and a high energy density is required.

1 Introduction

The concept of material development arises when designing critical infrastructures that require high performance at cryogenic and elevated temperatures. Such materials need to meet the functional and structural requirements to withstand harsher environmental conditions [1, 2]. A material of high entropy alloys AlTiZrNbVCr HEA was considered viable because of its low density and light weight, good machinability and excellent performance in extreme conditions [3, 4] Employing this material alongside cutting-edge methods like laser engineering net shape (LENS) facilitates the creation of robust structural components suitable for diverse engineering applications.

The first two researchers that discovered this HEA were Jien-Wei Yeh and Brian Cantor as early as 2004, and their research defined the alloy's composition with at least five major elements, while the atomic percentage of each element varies from 5-35%. [3, 5]. HEAs are

characterised as random solid solutions, which prevail over the intermetallic compounds and conventional alloys due to the high configurational entropy of mixing [6, 7]. Ideally, if these alloys assumed the solid solution features, the configurational entropy of mixing will increase with respect to an increase in the number of compositional elements and their concentration [8]. Additionally, HEAs are usually influenced by core effects [9] that may restrict the formation of intermetallic compounds, reduce the diffusion rate of atoms from variations in lattice potential energy, and the presence of a high number of elements can lead to a large lattice distortion [10, 11]. As the atoms of each element interact, their influence may have an impact on the HEA's behaviour [12]. All these factors were taken into consideration when designing the alloys in this study [13-15]. A design component made from this material must be structurally balanced so as to offer superior combinations of strength and ductility and be able to withstand applied loading without exhibiting excessive deflection and breaking in the lifecycle [16-18].

Harder materials tend to have more densely packed crystal structures, making it more resistant to corrosive agents' metal corrosion agents to penetrate and attack the underlying metal [19-21]. Often, manufacturing process parameters may indirectly affect corrosion behaviour by altering the microstructure of HEAs [22, 23]. Consequently, it affects their response to a specific environment such as alkalis, acids, temperature, and humidity. A smooth surface with fewer surface defects and roughness may exhibit better corrosion resistance by reducing the site for corrosion initiation [24-26].

With the emergence of high-entropy alloys (HEAs), their smooth surfaces with minimal surface defects have made this a material of interest in highly corrosive environment. This is because of the high entropy of mixing and the lattice distortion effect, which enhance the strength while also preventing plastic deformation and dislocation movement [15, 27]. As such, it will culminate in a reduction in wear loss and an increase in wear resistance [28]. [28]. In the present study, the microstructural characterization, hardness and corrosive behaviour of AlTiZrNbVCr HEA was investigated.

The process parameters, such as laser power, scan speed, hatch distance, layer thickness and heat (temperature gradient) can significantly influence the hardness, microstructure, and corrosion behaviour of alloys. For example, an increase in the scan speed may reduce the laser-material interaction time and lower the energy per unit volume, potentially causing incomplete melting. Conversely, increasing laser power can create a steep temperature gradient, which accelerates corrosion. The key is to carefully adjust laser parameters to achieve a balance between microstructural grain refinement and phase composition changes, which ultimately dictates the alloys hardness and corrosion resistance, as observed in Ti6Al4V[29]

Building orientation in additive manufacturing (AM) significantly affects microstructural distribution and mechanical properties, mainly because of its impact on heat transfer, cooling rate, and grain structure [30]. Different building orientations can create variations in heat transfer modes and efficiencies. These variations lead to differences in cooling rates, which control grain size, texture, and phase formation. Higher cooling rates associated with certain orientations produce finer grains and stronger interlayer metallurgical bonding. This improves hardness, surface quality, and tensile strength. The cooling rate also influences microstructure formation, including precipitate size and distribution, which have a strong impact on hardness and corrosion resistance. Rapid cooling usually increases the nucleation rate but limits diffusion [31] . This leads to a higher number of small precipitates that hinder dislocation movement, which enhances hardness due to increased precipitation. Additionally, processing methods that increase high-angle grain boundaries and reduce grain size tend to improve corrosion resistance by forming denser passive films.

2 Material and methods

In this study, AlTiZrNbVCr HEA powder (99.8% purity) with a grain size of 45 µm was selected, mixed and homogenized for 8 hours in a 3D tubular mixer (T2 GE). The mixed powder was prepared through the LASER using a LENSTM 850R system with a 1 KW IPG fibre while the laser melt was deposited on a titanium substrate of 6.5 mm (thickness). The processing parameters were set as in **Table 1.** Each sample was characterised with a JEOL JSM-6510 scanning electron microscope (SEM) equipped with an energy dispersion spectrometer (EDS). The X-ray diffraction system used was an Analytical XPERT-PROX with a radiated CU-Ka and λ=1.54056Å. A nanoindentation test was conducted using a diamond pyramid Berkovich indenter via the Oliver-Pharr method to determine the hardness properties of the HEAs [32, 33] A simulation of solidification and SEM images using a computational tool (ATEX -software) to analyse the microstructural images was carried out. To determine the passivation behaviour of AlTiZrNbVCr HEA at room temperature, potentiodynamic polarization experiments were carried out using the electrochemical system (computer-controlled auto-lab potentiostat, PGSTAT302). A scanning rate of 1 mV. s^{-1} in a solution of 3.5 wt.% NaCl at room temperature was recorded. The experiment was performed with a three-electrode configuration cell system for an hour under atmospheric control (nitrogen gas) so as to prevent the effect of oxidation. In this case, AgCl/Ag and platinum rods were used as reference electrodes and counter electrodes, respectively, and the fabricated sample was used as the working electrode. Before and after analyses, the samples were washed with distilled water, degreased with acetone, and air (dried). Using a working electrode, a sample with a surface area of 100 mm^2 was exposed to electrolytes for 20 hours during the electrochemical test.

Table 1. Laser parameters used in the melting processes.

Sample	Chemical Composition	Laser Power, (W)	Scan Speed (mm/s)	Hatch Spacing (mm)	Layer Thickness (mm)	Laser Spot size (mm)	Energy Density/ mm^3
A	$Al_{10.77}Ti_{46.98}V_{12.39}Nb_{14.16}Zr_{11.23}Cr_{4.47}$	300	10.16	0.660	0.30	1.35	149
B	$Al_{10.07}Ti_{53.16}V_{11.22}Nb_{11.87}Zr_{9.32}Cr_{4.36}$	360	8.64	0.660	0.30	1.35	186
C	$Al_{8.56}Ti_{46.46}V_{12.39}Nb_{17.84}Zr_{10.48}Cr_{4.27}$	300	8.64	0.660	0.30	1.35	175

3 Result and discussion

3.1.1 SEM analysis

A laser power of 360 W significantly affects the temperature of molten pools and depth, as well as the microstructure and mechanical characteristics of alloys. Therefore, a higher

energy melting typically leads to a large columnar grain structure because of the increased in energy input, thereby creating a larger and deeper melt pool. In contrast, remelting generates more layers, thus, promoting epitaxial grain growth and a refined microstructure. At 360W (8.64 mm/s), a solid solution BCC matrix with a B2 secondary phase will evolve. In this case, the melting efficiency was increased, resulting in a more uniform and homogeneous microstructure with fewer cracks.

In solidification processes, the temperature gradient typically represents the most rapid temperature increase and is usually aligned with the direction of heat flow towards the melt, thereby corresponding to the direction of grain growth in the solidified microstructure.
SEM images of HEAs shown in **Fig. 1** revealed that their solidification rate (rapid cooling) increases with a reduction in temperature gradient, thereby forming a transitional columnar grain. With the increase in temperature gradient. The thermal energy generated by deposition increased the crystallization of the HEA microstructure, while the previously generated thermal energy enhanced the deposited layer of the molten metals of HEA. This change will enhance bonding between layers, reduce porosity, and also improve phase formation and grain growth. Sample **1A** displayed a relatively coarse, irregular texture with isolated light and dark regions. In addition, there is evidence of a porous and dendritic solidification structure with multiple phases present. Sample **1B** shows some texture features with roundish in a well-separated region. The bright spots indicate the presence of secondary BCC phases that nucleate within the matrix. Sample **1C** presents a uniform, fine-grained structure with a dense honeycomb pattern. This structure is typical of spinodal decomposition in BCC+B2 phases. Moreover, the structure is uniform due to the rapid solidification that occurs [34].

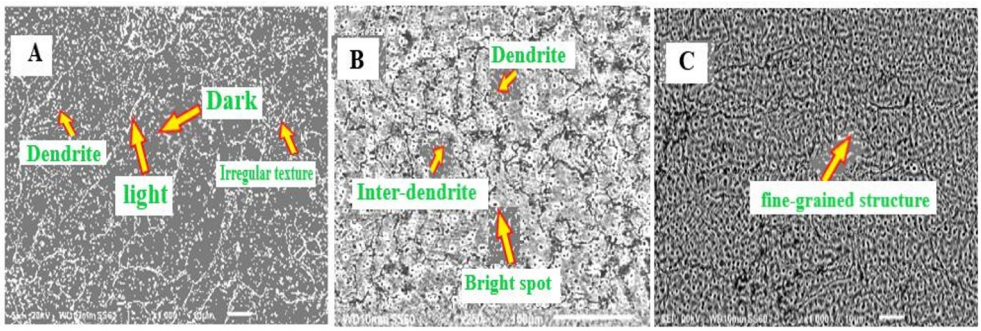

Fig. 1. SEM images (A, B, C and D) of the microstructure of AlTiZrNbVCr HEA.

The extremely rapid cooling caused uneven contraction in the HEAs, generating internal stresses. In microscopic analysis, the grain boundary changes its orientation with respect to neighbouring grains. In this case, mapping of crystallographic orientation was carried out to determine the position and characteristics of grain boundaries. The structure that evolved exhibits a significant change in the grain boundary plane, which is inclined perpendicular to the growth direction. There is segregation of solute composition at the grain boundary due to the depletion of some light elements such as Al, Ti, and V. The strong repulsive interaction of other elements in the solid solution with aluminium promotes depletion at the grain boundary [35]. Some inhomogeneous segregation patterns of solute composition occur at the grain boundary plane. Most BCC elemental compositions were enriched with dendritic cores, and the B2 elements are segregated into intermetallic regions. A B2 phase intermetallic is separated and formed during the solidification, this is because B2 phases have little solubility in the BCC phase [36].

Figure 2 illustrates the distribution of constituent elements Al-Ti-Zr-Nb-V-Cr overlaid onto the SEM image. A mapping of elemental composition was determined using the energy-dispersed spectroscope (EDS) on the as-built alloys (from laser melting and deposition).

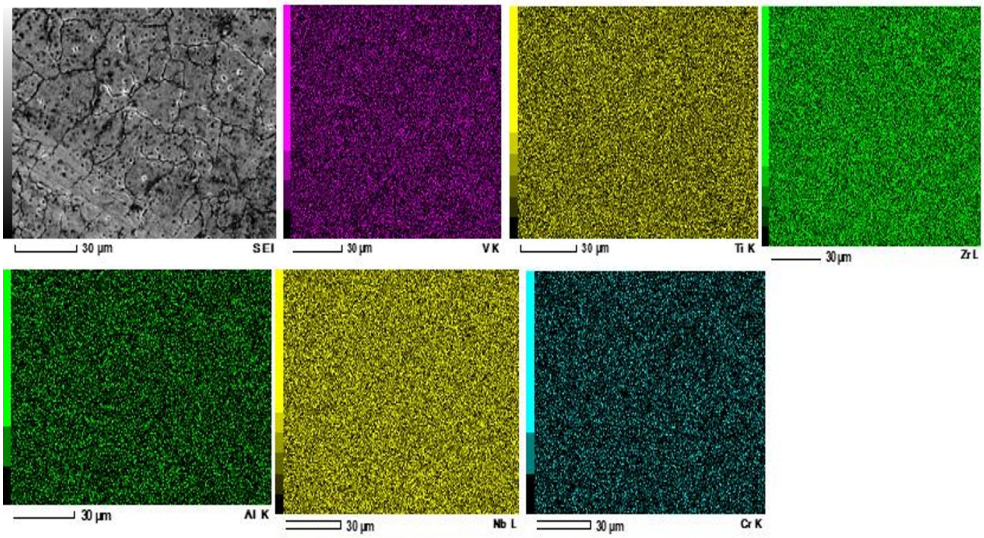

Fig. 2. SEM-EDS elemental mapping images of Al-Ti-Zr-Nb-V-Cr HEA.

The micrograph depicts SEM-EDS images of elemental maps for HEAs, which illustrate the spatial distribution of the chemical compositions of aluminium, titanium, zirconium, niobium, vanadium, and chromium. A visible structure made up of polygonal grains separated by well-defined grain boundaries was featured. While some observed contrast variation within grains indicates the presence of compositional inhomogeneities at the sub-grain level.

In the elemental mappings, the compositional elements (AlTiZrNbVCr) have a very uniform distribution of their constituent elements. Furthermore, there is no discernible segregation, precipitate, or elemental clustering. This suggests that the alloys are homogeneous and probably single-phase. Additionally, the principal elements are well distributed, and no evidence of phase separation was observed. One advantage of this structural HEA is that the structural HEA provides enhanced mechanical properties and corrosion resistance due to the absence of chemical segregation. Its uniformity suggests that high hardness and wear resistance are also attainable.

3.1.2 Fast Fourier Transform (FFT) analysis

In the analysis of microstructures, there may be some complex SEM images with intricate features that may not clearly be visible but will require a high resolution in order to analyse crystal orientation and other features. In this case, the computational software tool ATEX, Digital Micrograph (DM), was used. The SEM micrographs (**Fig. 3**) of the HEAs were analysed to explore the underlying characteristic length scale of dendrite, and the SEM images obtained were transformed into a Fast Fourier Transform (FFT) processing (**Fig. 4A**).

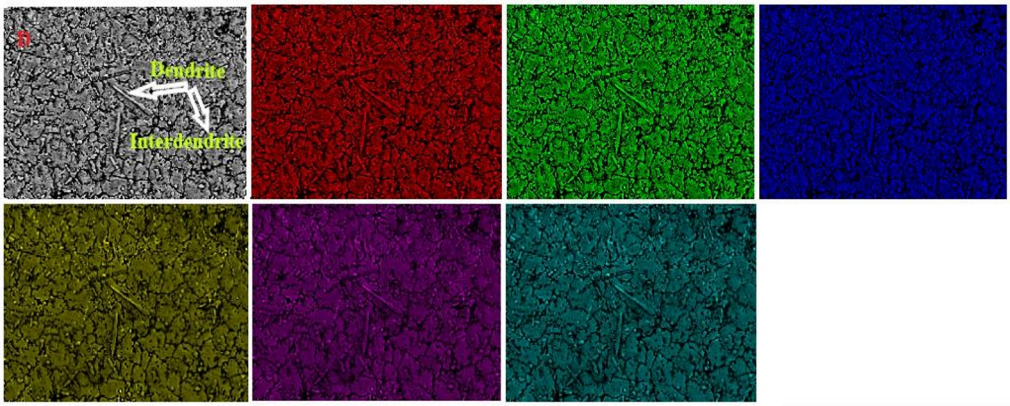

Fig. 3. SEM-EDS elemental mapping images of a dendrite in the HEAs.

Moreover, the typical size of the dendrite structure was sparsely visible because of a mix of different wavelengths in the power spectrum and intensity profile, which was caused by background noise and a weak frequency signal.

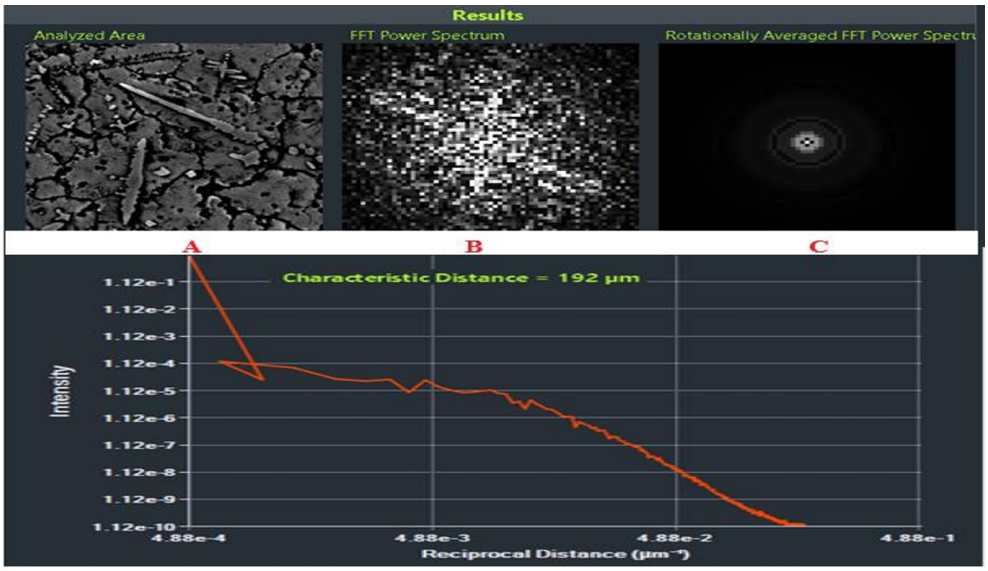

Fig. 4 A Fast Fourier Transform applied to the processing of a dendrite in the HEAs.

Nonetheless, a rotational average process was applied to enhance the noises and signals. As such, evidence of scattering at the peak with each characteristic frequency was displayed. Besides, the results show the BCC crystal grew along the crystallographic direction.
As shown in **Fig. 4B**, the FFT power spectrum exhibits strong symmetry and bright spots, which is corroborated by the rotationally averaged FFT in **Fig. 4C.** This correspondence aligns with the axis of the BCC structure, thereby indicating a spatial alignment within the dendrite. The characteristic length scale of the dendrite structure (**Fig. 4D**) was determined to be LC 192µm. This length of the dendrite (dendrite arm spacing) has a significantly effect

on the mechanical performance of fabricated sample of HEAs. Densification of dendrite boundaries serves as an impedance to dislocation movement; as such, it enhances both yield strength and hardness. Therefore, any alloy with a refined structure usually displays better plastic strain, and this can be attributed to the uniform distribution of secondary phases and fine microstructures.

3.1.3 Crystallographic and phase analysis of HEAs

The diagram presents an X-ray diffraction pattern (**Fig. 5**) that analyses the crystallographic structure and phase composition of HEA. Each crystalline phase produces characteristic diffraction peaks at specific angles according to Bragg's law. These diffraction peaks are labelled with Miller indices (101, 211, 202, 220, 110, 114, 200, and 222). All samples showed metallic phases of Ti, Al_3Ti, and Al_9Cr_4, which were predominantly characterized by BCC crystal phases with the highest intensity at 46.259°, 40.153°, and 38.537°, corresponding to the (202), (114), and (200), while the respective interplanar distances were 3.3010 Å, 38.610 Å, and 2.9500 Å, respectively. Sample A displayed diffraction peaks with broader features, illustrating the reduced crystallinity. Sample B shows a sharp, intense peak; this sharpness is an indication of a well-crystallised and possibly single-phase. Samples B and C are identical and exhibit the same single phase with greater crystallinity. A sharp, intense peak in sample C, coupled with its consistent regularity, is an indication of a highly crystalline structure with a single phase. As a result, the arrangement of atoms is well-ordered, and this is evidence of a high purity and uniform composition.

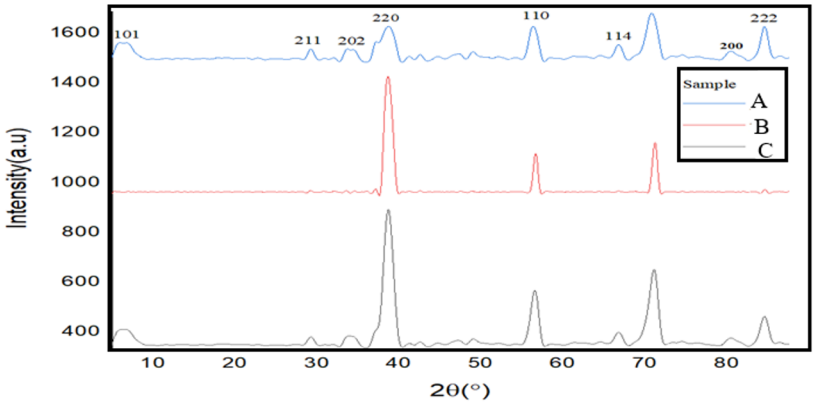

Fig. 5 XRD Spectrum of AlTiZrNbVCr HEA illustrating the phase evolution of BCC in samples A, B, and C.

3.1.4 Nano hardness

Figure 6 illustrates the relationship between applied load and indenter displacement during the nanoindentation test. Each curve consists of three distinct phases, such as loading, dwell time at peak load, and unloading. All three samples display a smooth increase in force with depth of up to about 400 mN and 1400 nm indentation depth. Sample A has the highest hardness and elastic modulus amongst the three and also exhibits greater elastic recovery and less permanent deformation, signifying a higher wear-resistance microstructure. Sample B displayed an intermediate mechanical response. This enhancement arises from interface strengthening, facilitated by element diffusion and structural transformation. Likewise, Song, Junhan, et al. (2024) [37] hold the view that diffusion and structural transformation can improve the strength of HEAs while sample C showed the lowest stiffness and hardness and exhibited the highest plastic deformation under the same maximum load, thus indicating the lowest elastic modulus.

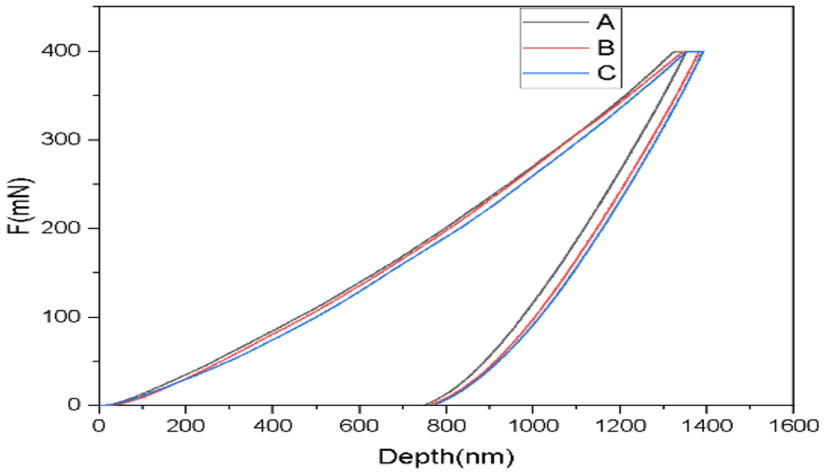

Fig.6. Nanoindentation load displacement curves Al-Ti-Zr-Nb-V-Cr of the HEA deposit.

3.1.5 Corrosion resistance

The results in **Fig. 7** show a stable value after measuring an open-circuit potential (OCP) of -0.5V for 15 min. The passivation region in NaCl was formed as a result of the presence of chromium [38]. The presence of Al in AlTiZrNbVCr HEAs matrix reduces the density of HEA since it is a low-density element. Aluminium is also at a lower stage in the galvanic series when compared to other elements in HEAs [Cr, Nb, Ti, Zr and V (noble)], and therefore it is feasible that Al atoms may preferentially be release from the solid solution which contains more noble elements in an aqueous NaCl environment.

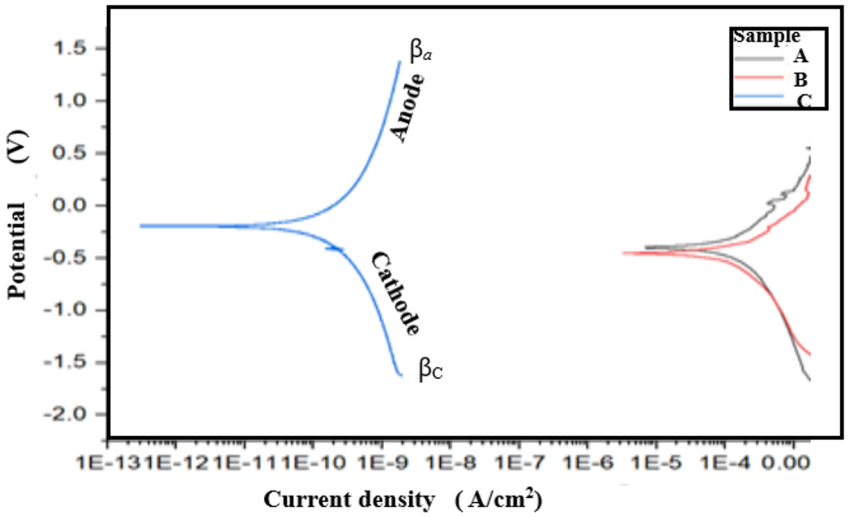

Fig. 7. Potentiodynamic polarization curves of AlTiZrNbVCr in NaCl solution at room temperature.

The polarization curves for samples A, B, and C reveal their behaviour in a corrosive environment, based on current density (A/cm²). Sample C exhibited a very low current density across a wide range of potentials, with its anodic current sharply increasing only at approximately 1E-9 A/cm², indicating high corrosion resistance. Conversely, samples A and B displayed high current densities at similar potentials, suggesting a higher corrosion rate and lower corrosion resistance due to their anodic current occurring at much higher current densities.

The Tafel equation is expressed as follows:

$$\boldsymbol{\eta = \pm A\, log_{10}\left(\frac{i}{i_0}\right)} \tag{1}$$

Where η denotes overpotential in V, A indicates Tafel slope in V, i is the current density (A/m²), i_0 is expressed as exchange current density in A/m², and +/- indicates an anodic and cathodic process

The symbols in Table 2, representing the cathodic (β_C), anodic (βa), and Tafel slope, respectively, the corrosion potential (Ecorr,) the corrosion current (Jcorr), the polarization resistance (Rp), and the corrosion rate (Rcorr). The Tafel extrapolation graphs were generated from corrosion (rate) tests performed. This test was performed using ASTM G3 to achieve the Tafel extrapolation graph [39]. The average corrosion current density values (Icorr) for both the anodic slope (βa) and cathodic slope (βc) and the corrosion potential (Ecorr) were calculated from the Tafel extrapolation.

$$R_P = \frac{1}{J_{CORR}}\left(\frac{\beta_C\,\beta_a}{2.3\beta_C+\beta_a}\right) \tag{2}$$

$$R_{CORR} = J_{CORR}\left(\frac{K\ x\ E_W}{d\ x\ A}\right) \tag{3}$$

Table 2 Anodic and cathodic slope.

	Corrosion current	Anodic Slope	Cathodic slope	E_{corr} Corrosion Potential
	Ecorr (V)	βa (V)	βc (V)	I_{corr} (μA/cm^2)
A	0.219	1.703	1.387	0. 244
B	0.355	0.610	1.021	2.446
C	0.410	0.846	1.506	1.322

The corrosion resistance increases from samples A, B, and C, where sample C has the highest corrosion resistance when compared with the other two samples. The addition of the Nb element composition in Sample C, compared to Samples A and B, significantly improves corrosion resistance. This is because a higher Nb content usually promotes the formation of a stable, dense oxide (Nb_2O_5) film on the alloy's surface. These films act as a protective layer against corrosive media, thus preventing further oxidation and material degradation. The presence of vanadium, titanium, chromium, and aluminium in oxide form (Al_2O_3, TiO_2, and V_2O_3) also supports the film's stability and integrity.

4 Conclusion

Our study examined the hardness, microstructure, and corrosion resistance of AlTiZrNbVCr high entropy alloys.
Images obtained from SEM analysis revealed that HEAs solidify faster at a lower temperature gradient. But as the temperature gradient increases, the thermal energy generated by deposition also increase because a large difference in temperature drives more intense heat flow from the hottest region to the cold region. As such it promotes the crystallization of the HEA microstructure.

The Fast Fourier Transform (FFT) SEM processing image shows that the BCC crystal grew in the crystallographic direction as shown in the distinct symmetry and bright spots.
The result shows that sample A has the highest hardness and wear-resistant microstructure when compared with the other samples (B and C). Thus, the laser power and energy density significantly impacted the mechanical properties of the HEA tested.

The presence of aluminium composition in the HEAs helps stabilise the solid solution of a BCC structure. These alloys exhibit a high corrosion resistance due to the characteristic nature of each element that facilitates the formation of a passive layer due to the presence of Al and Cr that form a stable oxide (Al_2O_3 and Cr_2O_3). Since the passivation was spontaneous even at standard temperature and pressure (STP). Therefore, sample A exhibits a low corrosion rate when compared with other samples B and C, and this was attributed to the formation of a protective passive film.

The authors would like to thank the Surface Engineering Research Laboratory (SERL) at Tshwane University of Technology's Department of Chemical, Metallurgical, and Material Engineering and the Council for Scientific and Industrial Research (CSIR), Pretoria, South Africa.

References

1 Fang, Y., Hu, Z., Ji, J., Sun, L., Wang, L., and Zhan, X.: ‘Preparation of a novel high-entropy alloy AlNbTiVZr with excellent strength and ductility: The effect of Zr composition on microstructure and properties’, Materials Science and Engineering: A, 2024, **918**, 147441 https://doi.org/10.1016/j.msea.2024.147441

2 Liang, J., Li, G., Ding, X., Wen, Z., Zhang, T., Li, Y., and Qu, Y.: 'Formation of Zr-rich BCC phase and its relation to the hydrogen storage properties of TiVNbZr high entropy alloy', International Journal of Hydrogen Energy, 2023, **48**, (86), 33610-33619 https://doi.org/10.1016/j.ijhydene.2023.05.100

3 Pandey, V., Seetharam, R., and Chelladurai, H.: 'A comprehensive review: Discussed the effect of high-entropy alloys as reinforcement on metal matrix composite properties, fabrication techniques, and applications', Journal of Alloys and Compounds, 2024, **1002** 175095 https://doi.org/10.1016/j.jallcom.2024.175095

4 Ren, J., Kumkale, V.Y., Hou, H., Kadam, V.S., Jagtap, C.V., Lokhande, P.E., Pathan, H.M., Pereira, A., Lei, H., and Liu, T.X.: 'A review of high-entropy materials with their unique applications', Advanced Composites and Hybrid Materials, 2025, **8**, (2),. 195 https://doi.org/10.1007/s42114-025-01275-4

5 Yadav, D.K., Mandal, A.B., Sharde, P., Marandi, L., and Sinha, S.: 'Journal of Alloys and Metallurgical Systems', Journal of Alloys and Metallurgical Systems, 2024, **7**,. 100100 https://doi.org/10.1016/j.jalmes.2025.100170

6 Caramarin, S., Badea, I.-C., Mosinoiu, L.-F., Mitrica, D., Serban, B.-A., Vitan, N., Cursaru, L.-M., and Pogrebnjak, A.: 'Structural Particularities, Prediction, and Synthesis Methods in High-Entropy Alloys', Applied Sciences, 2024, **14** (17), 7576 https://doi.org/10.3390/app14177576

7 Anand, A.: 'Defect energetics and deformation mechanisms in refractory high entropy alloys', University of Toronto (Canada), 2024

8 Li, X., Zou, Y., Lu, H., and Wang, L.: 'Nanoscale high-entropy alloys for solar and thermal applications', Nanoscale, 2025 **17**,6266-6286 https://doi.org/10.1039/d4nr04697h

9 Verma, P.K., and Vasudev, H.: 'Performance of High-Entropy Alloy Coatings Sprayed Using Plasma Spraying Technique': 'Thermal Spray Coatings for High-Temperature Conditions' (CRC Press). 259-275 ISBN9781003542957

10 Hsu, W.-L., Tsai, C.-W., Yeh, A.-C., and Yeh, J.-W.: 'Clarifying the four core effects of high-entropy materials', Nature Reviews Chemistry, 2024, **8**, 471–485 https://doi.org/10.1038/s41570-024-00602-5

11 Woodgate, C.D., Naguszewski, H.J., Redka, D., Minár, J., Quigley, D., and Staunton, J.B.: 'Emergent B2 chemical orderings in the AlTiVNb and AlTiCrMo refractory high-entropy superalloys studied via first-principles theory and atomistic modelling', arXiv preprint arXiv:**2503**.13235, 2025 https://doi.org/10.48550/arXiv.2503.13235

12 Ma, E., and Ding, J.: 'Compositional fluctuation and local chemical ordering in multi-principal element alloys', Journal of Materials Science & Technology, 2025, **220**,. 233-244 https://doi.org/10.1016/j.jmst.2024.09.008

13 Dangwal, S., and Edalati, K.: 'Developing a single-phase and nanograined refractory high-entropy alloy ZrHfNbTaW with ultrahigh hardness by phase transformation via

high-pressure torsion', Journal of Alloys and Compounds, 2025, **1010**, 178274 https://doi.org/10.1016/j.jallcom.2024.178274

14 Song, Y., Chang, Z., Ge, Y., and Bi, W.: 'Effect of deposition strategies on the thermo-mechanical behaviour of selective laser melting Al0. 5CrCoFeNi high-entropy alloy, Materials Today Communications, 2025, **42**, 111386 https://doi.org/10.1016/j.mtcomm.2024.111386

15 Wang, H., Yang, P., Zhao, W., Ma, S., Hou, J., He, Q., Wu, C., Chen, H., Wang, Q., and Cheng, Q.: 'Lattice distortion enabling enhanced strength and plasticity in high entropy intermetallic alloy', Nature Communications, 2024, **15**(1). 6782 https://doi.org/10.1038/s41467-024-51204-0

16 Nene, S., Sinha, S., Yadav, D., and Dutta, A.: 'Metallurgical aspects of high entropy alloys', Journal of Alloys and Compounds, 2024, **1005** 175849 https://doi.org/10.1016/j.jallcom.2024.175849

17 Abdullah, M.R. and Peng, Z., 2024. Review and perspective on additive manufacturing of refractory high entropy alloys. Materials Today Advances, **22**, ISSN 2590-0498 100497.https://doi.org/10.1016/j.mtadv.2024.100497

18 Li, Y., Liang, S., Gong, J., Wu, W., Wang, Y., and Chen, Z.: 'Effect of Ti on the structure and mechanical properties of TixVNbMo (x= 0.5, 1.0, 1.5, 2.0) refractory high-entropy alloys: A combined first principles and experimental study', Intermetallics, 2025, **181** (19), 108760 https://doi.org/10.1016/j.intermet.2025.108760

19 Liu, C., Wang, Y., Zhang, Y., Zhang, L.-C., and Wang, L.: 'Deformation mechanisms of additively manufactured TiNbTaZrMo refractory high-entropy alloy: The role of cellular structure', International Journal of Plasticity, 2024, **173**. 103884 https://doi.org/10.1016/j.ijplas.2024.103884

20 Cabrera, M., Oropesa, Y., Sanhueza, J.P., Tuninetti, V., and Oñate, A.: 'Multicomponent alloys design and mechanical response: From high entropy alloys to complex concentrated alloys', Materials Science and Engineering: R: Reports, 2024, **161**, 100853 https://doi.org/10.1016/j.mser.2024.100853

21 Liang, J., Cao, G., Zeng, M., and Fu, L.: 'Controllable synthesis of high-entropy alloys', Chemical Society Reviews, 2024, **53**, 6021–6041 https://doi.org/10.1039/d4cs00034j

22 Meng, Y., Yang, Z., Shi, Y., Liu, X., Wang, L., Zhang, Q., and Yao, J.: 'Microstructural evolution and enhanced properties of multi-layer TiZrNbCrCo high entropy alloy coatings laser-clad onto Ti–6Al–4V alloy', Intermetallics, 2024, **173**, 108407 https://doi.org/10.1016/j.intermet.2024.108407

23 Lian, X., Cui, H., Song, X., Zhao, J., and Yang, X.: 'Tailoring the amorphous-nanocrystalline structures of TiNbZrNx films towards improving the anti-corrosion and mechanical properties by controlling nitrogen flow ratio', Surface and Coatings Technology, 2024, **476**, 130274 https://doi.org/10.1016/j.surfcoat.2023.130274

24 Cui, C., Xu, H., Yang, J., Cui, X., and Lu, J.: 'Effects of Al variations on the microstructure and mechanical properties of laser-cladding $Al_xNbMo_{0.5}Ti_{1.5}Ta_{0.5}Cr_{0.5}$ refractory high-entropy alloy coatings', Journal of Alloys and Compounds, 2025, **1010**. 177445 https://doi.org/10.1016/j.jallcom.2024.177445

25 Yu, K., Li, Z., Zhou, F., Li, Y., Tang, J., and Luo, Z.: 'Effect of C content on the microstructural evolution and wear resistance of AlCoCrFeNiTiW high-entropy alloy coatings', Surface and Coatings Technology, 2025, **505**,132115 https://doi.org/10.1016/j.surfcoat.2025.132115

26 Qi, M., Cui, X., Jin, G., Zhang, Q., Wang, Z., Liu, C., and Zhang, X.: 'Microstructure and properties of a multilayered laser cladding $Al_{0.2}NbTiV_{0.1}W_{0.5}Zr_{0.3}$ high-entropy alloy coating on a zirconium alloy', Surface and Coatings Technology, 2024, **477,** 130299 https://doi.org/10.1016/j.surfcoat.2023.130299

27 Cui, C., Xu, H., Ye, F., Yang, J., and Cui, X.: 'Microstructure evolution and characteristics of laser cladding with pre-placed powder lightweight refractory $Nb_xMo_{0.5}Ti_{1.5}Ta_{0.2}Cr$ high-entropy alloy', Intermetallics, 2024, **167**, 108229 https://doi.org/10.1016/j.intermet.2024.108229

28 Xu, T., Chen, Q., Ji, L., Zheng, Z., Wang, K., and Liu, H.: 'BCC/B2 structure and dislocation strengthening behaviour in high Ti content TiAlVCrNb high-entropy alloys', Journal of Alloys and Compounds, 2023, **956**, 170179 https://doi.org/10.1016/j.jallcom.2023.170179

29 Ni, C., Zhu, J., Zhang, B., An, K., Wang, Y., Liu, D., Lu, W., Zhu, L. and Liu, C., 2025. Recent advance in laser powder bed fusion of Ti–6Al–4V alloys: microstructure, mechanical properties and machinability. Virtual and Physical Prototyping, **20**(1), e2446952.https://doi.org/10.1080/17452759.2024.2446952

30 Du, Y., Xiong, J., Wen, G., Li, J., Jin, F., Zhang, H. and Wang, G., 2022. Microstructure and mechanical properties of Ti2AlNb diffusion bonding using multi-phase refractory high-entropy alloy interlayer. Materials Science and Engineering: A, **836**, .142688.https://doi.org/10.1016/j.msea.2022.142688

31 Liu, S., Cao, J., Zhou, Y., Hou, C., Dai, S. and Huang, X., 2022. Microstructure evolution and mechanical properties of a high-strength Ti2AlNb alloy processed by large-strain two-pass hot extrusion. Journal of Alloys and Compounds, **925**, .166715.https://doi.org/10.1016/j.jallcom.2022.166715.

32 Pharr, G.M., Herbert, E.G. and Gao, Y., 2010. The indentation size effect: a critical examination of experimental observations and mechanistic interpretations. Annual Review of Materials Research, **40** (1), 271-292 https://doi.org/10.1146/annurev-matsci-070909-104456

33 Zhang, H., Wu, M., Rodrigues, C.M., Ludwig, A. and Kharicha, A., 2021. Directional solidification of AlSi7Fe1 alloy under forced flow conditions: effect of intermetallic phase precipitation and dendrite coarsening. Metallurgical and Materials Transactions A, **52**(7),.3007-3022.https://doi.org/10.1007/s11661-021-06295-5

34 Zhang, X., Wan, Y., Chen, C. and Zhang, L., 2024. The effect of solute elements co-segregation on grain boundary energy and the mechanical properties of aluminium by first-principles calculation, Nanomaterials,**14**(22), 1803.https://doi.org/10.3390/met13040751

35 Devaraj, A., Wang, W., Vemuri, R., Kovarik, L., Jiang, X., Bowden, M., Trelewicz, J.R., Mathaudhu, S. and Rohatgi, A., 2019. Grain boundary segregation and intermetallic precipitation in coarsening-resistant nanocrystalline aluminium alloys. Acta Materialia, **165** 698-708**.**https://doi.org/10.1016/j.actamat.2018.09.038

36 Kube, S.A., Frey, C., McMullin, C., Neuman, B., Mullin, K.M. and Pollock, T.M.,2024. Navigating the BCC-B2 refractory alloy space: Stability and thermal processing with Ru-B2 precipitates. Acta Materialia, **265**, .119628. https://doi.org/10.1016/j.actamat.2023.119628

37 Song, J., Zhang, J., Peng, J., Song, X., Liang, L. and Feng, H., 2024. Mechanical properties and deformation behaviour of a high entropy alloy with precipitate under cycle loading. Frontiers in Materials, **11,** 1436577. 2024 https://doi.org/10.3389/fmats.2024.1436577

38 Zhang, L.N., Xiong, X.L., Yan, Y., Gao, K.W., Qiao, L.J. and Su, Y.J., 2019. Atomic modelling for the initial stage of chromium passivation. International Journal of Minerals, Metallurgy, and Materials, **26** (6), .732-739. https://doi.org/10.1007/s12613-019-1803-z

39 ASTM G3-14, Standard Practice for Conventions Applicable to Electrochemical Measurements in Corrosion Testing, ASTM International. West Conshohocken (2014).